


Cite this: *Catal. Sci. Technol.*, 2021, 11, 2433

Platinum and cobalt intermetallic nanoparticles confined within MIL-101(Cr) for enhanced selective hydrogenation of the carbonyl bond in α,β -unsaturated aldehydes: synergistic effects of electronically modified Pt sites and Lewis acid sites†

Muhammad Zahid,^a Jiang Li,^a Ahmed Ismail,^a
Francisco Zaera ^{*b} and Yujun Zhu ^{*a}

Precious metals have been shown to play a vital role in the selective hydrogenation of α,β -unsaturated aldehydes, but still suffer from challenges to control selectivity. Herein, we have advanced the design of catalysts made out of Pt–Co intermetallic nanoparticles (IMNs) supported on a MIL-101(Cr) MOF (3%Pt%Co/MIL-101(Cr)), prepared by using a polyol reduction method, as an effective approach to enhance selectivity toward the production of α,β -unsaturated alcohol, the desired product. XRD, N₂ adsorption–desorption, FTIR spectroscopy, SEM, TEM, XPS, CO adsorption, NH₃-TPD, XANES and EXAFS measurements were used to investigate the structure and surface properties of our 3%Pt%Co/MIL-101(Cr) catalysts. It was found that the Co-modified 3%Pt%Co/MIL-101(Cr) catalysts can indeed improve the hydrogenation of cinnamaldehyde (CAL) to cinnamyl alcohol (COL), reaching a higher selectivity under mild conditions than the monometallic Pt/MIL-101(Cr) catalysts: 95% conversion of CAL with 91% selectivity to COL can be reached with 3%Pt%Co/MIL-101(Cr). Additionally, high conversion of furfural (97%) along with high selectivity to furfural alcohol (94%) was also attained with the 3%Pt%Co/MIL-101(Cr) catalyst. The enhanced activity and selectivity toward the unsaturated alcohols are attributed to the electronic and geometric effects derived from the partial charge transfer between Co and Pt through the formation of uniformly dispersed Pt–Co IMNs. Moreover, various characterization results revealed that the addition of Co to the IMPs can promote the Lewis acid sites that facilitate the polarization of the charge-rich C=O bonds and their adsorption *via* their oxygen atom, and also generate new interfacial acid sites.

Received 26th October 2020,
Accepted 22nd January 2021

DOI: 10.1039/d0cy02082f

rsc.li/catalysis

1. Introduction

The selective hydrogenation of unsaturated aldehydes, especially of α,β -unsaturated aldehydes, is a valuable route for the synthesis of unsaturated alcohols, important intermediates in the fabrication of fine chemicals like flavours, fragrances and pharmaceutical compounds.^{1–3} Nonetheless, this reaction involves complex reaction networks, such as in the case of the hydrogenation of

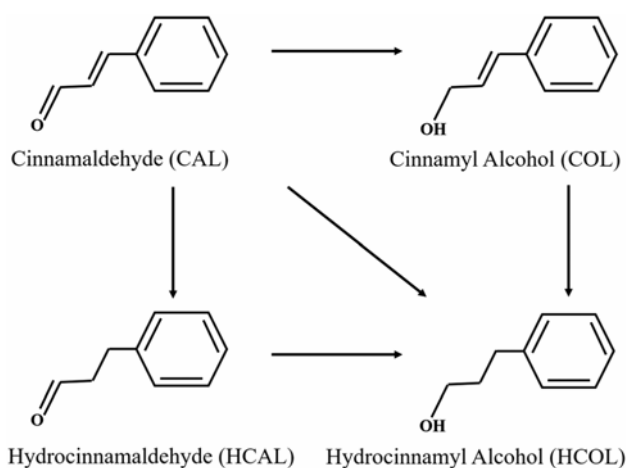
cinnamaldehyde (CAL) shown in Scheme 1, which include competitive reduction steps at either of the two unsaturated groups of α,β -unsaturated aldehyde, *i.e.*, the carbonyl bond (C=O) and the conjugated olefin bond (C=C). Thermodynamically, the hydrogenation of C=C bonds is more favorable than that of C=O bonds, making it extremely difficult to attain high selectivity toward C=O bond hydrogenation to produce unsaturated alcohols. It is quite challenging, from either economic or scientific points of view, but highly desirable to improve the selectivity of these reactions to make unsaturated alcohols.^{1,4–7} Generally, the hydrogenation of C=O bonds is not easy to promote and often requires supported catalysts with both mono- or bimetal nanoparticle catalysts as well as Lewis acid sites operating under high temperatures and high hydrogen pressures.^{8–11} Alternatively, such a hydrogenation may be possible *via* transfer hydrogenation with an alcohol as a hydride donor.⁷

Heterogeneous catalysts have been the most commonly used for selective catalytic hydrogenation.^{12–15} These

^a Key Laboratory of Functional Inorganic Material Chemistry, Ministry of Education of the People's Republic of China, Heilongjiang University, Harbin, 150080, China. E-mail: yujunzhu@hlju.edu.cn; Tel: +86 45186609650

^b Department of Chemistry and UCR Center for Catalysis, University of California, Riverside, 900 University Avenue, Riverside, California 92521, USA. E-mail: zaera@ucr.edu

† Electronic supplementary information (ESI) available: FTIR spectra, SEM image, XPS characterization, CO adsorption, NH₃-TPD, EXAFS fitting results, effects of reaction conditions on activity and comparison of the catalytic performances with other reported Pt-based catalysts. See DOI: 10.1039/d0cy02082f



Scheme 1 Reaction pathways for CAL hydrogenation.

heterogeneous catalysts comprise both transition metals (Co, Sn, Cu, Ni, *etc.*) and noble metals (Pt, Au, Pd, *etc.*). Improving the selectivity toward carbonyl (C=O) bond hydrogenation can be obtained with bimetallic catalysts, where one of the noble metals (frequently Pt) is combined with a more electropositive, *i.e.* electron deficient, transition metal (Co, Sn, Fe, Ni, Zn, *etc.*) to form intermetallic nanoparticles (IMNs).^{1,8,9,13,16–18} These IMN catalysts have attracted extensive research interest because of their higher catalytic selectivity towards unsaturated alcohols under mild reaction conditions, a behavior that has been ascribed to the synergetic effects and cooperative interactions between the individual metal components. Previous literature has also acknowledged that the geometric and electronic structures of IMNs play pivotal roles in the adsorption and activation of different functional groups during the selective hydrogenation of α,β -unsaturated aldehydes.^{1,8,9,13,16–26} The active noble metal (*e.g.* Pt, Pd, *etc.*) usually facilitates the adsorption and dissociation of both hydrogen and the substrate (an α,β -unsaturated aldehyde), whereas the second electron-deficient metal (*e.g.* Co, Sn, Zn, Ga, In, *etc.*) modifies and adjusts the surface electronic structure of the noble metal *via* electron transfer, and with that shifts the relative reactivity toward the desired functional groups.

In addition to considerations regarding the active metallic phase, the choice of support is fundamental to improve the durability and reaction activity of these hydrogenation catalysts and, most importantly, their selectivity toward the desired C=O hydrogenation (which they can presumably modify *via* strong metal–support interactions (SMSIs)). Typical supports used for these catalysts include metal oxides such as acidic Al₂O₃, Fe₂O₃, and TiO₂, inert SiO₂, basic MgO, and carbon materials.^{2,11,13,14,27–31} The specific interactions between the supports and the IMNs may lead to distinctive hydrogenation reaction results because of adjustments to the electronic and geometric properties of the catalysts.³²

One promising family of well-defined supports are metal-organic frameworks (MOFs). These are composed of metal ions or metallic clusters connected by bi- or multipodal organic

ligands, forming three-dimensional well-defined zeo-type structures.^{33,34} They have attracted extensive research interest because of their high surface area, low density, and tunable pore size from micro- to meso-pores and 3D structure, all properties that may be tuned for potential applications in the fields of gas storage, adsorptive separation, sensing, and catalysis.^{33–36} A particularly interesting MOF is MIL-101(Cr), which is assembled *via* chromium metal ions connected by terephthalic acid. This MOF was initially synthesized by Ferey *et al.*,³⁷ who demonstrated its high thermal stability, chemical stability, acid–base resistance, large surface area and mesoporous structure³⁸ and successfully used it as a catalyst support in heterogeneous catalysis.^{37–40} The water molecules that are coordinated to the chromium centres in this MOF can be easily removed at elevated temperature under vacuum, thus producing unsaturated chromium (Cr(III)) Lewis acid sites accessible for potential adsorption of α,β -unsaturated aldehyde molecules.^{36,40,41} These characteristics of MIL-101(Cr) make it an ideal host for selective hydrogenation catalysis. MIL-101(Cr) can accommodate intermetallic nanoparticles, and the connecting window can provide access for the diffusion of α,β -unsaturated aldehydes to reach the metal active sites encapsulated in MIL-101(Cr) for catalytic reactions. There is only a limited number of citations in the literature on the use of MOF supports for the selective hydrogenation of α,β -unsaturated aldehydes,^{9,10,33,40–45} and, to the best of our knowledge, MIL-101(Cr) as a support for metal nanoparticles has only been reported sparingly,^{40–42} in particular for the selective hydrogenation of cinnamaldehyde (CAL) and furfural (FFL), where the selective hydrogenation of the olefinic (C=C) bonds was reported. We hypothesized that MIL-101(Cr) can be a great support for the dispersion of metal nanoparticles to improve the selectivity toward unsaturated alcohols in the hydrogenation of CAL and FFL under ambient reaction conditions. We combine that premise with the idea of using intermetallic nanoparticles as a way to tune the electronic properties of the active phase.

By taking into consideration the previous findings discussed above, in the work reported here we prepared a series of Pt–Co intermetallic nanoparticles confined within the pores of MIL-101(Cr) (3%Pt_y%Co/MIL-101(Cr) $y = 1, 3, 5$) made by a simple polyol reduction method without using any additional stabilizing agent. The 3%Pt3%Co/MIL-101(Cr) catalyst made this way showed particularly good catalytic selectivity for the hydrogenation of CAL and FAL, performing as an efficient and easily recyclable catalyst for the low-cost and eco-friendly production of unsaturated alcohols (cinnamyl alcohol (COL) and furfural alcohol (FOL), respectively). The effect of Co in modifying the behavior of the Pt surface and the properties of the MIL-101(Cr) support on activity and selectivity were investigated by using various characterization techniques.

2. Experimental

2.1. Preparation of MIL-101(Cr)

MIL-101(Cr) was prepared following a HF-free hydrothermal method reported in the literature.³⁴ The HF-free method was

chosen to avoid the toxic and highly corrosive nature of that acid. Briefly, $\text{Cr}(\text{NO}_3)_3 \cdot 9\text{H}_2\text{O}$ (5 mmol, 2.0011 g), terephthalic acid (5 mmol, 0.84 g) and deionized water (24 mL) were mixed at room temperature for about 30 min. The mixture was sonicated for an hour at room temperature in air. Then, the mixture was transferred into a 50 mL stainless steel autoclave coated with a Teflon inner layer and heated at 220 °C for 18 h without stirring. After crystallization, the resulting solid was cooled to room temperature. Finally, the green powder was precipitated by centrifugation, dried at 75 °C overnight, and heat-treated directly at 150 °C for 12 h under vacuum to obtain the MIL-101(Cr) support.

2.2. Preparation of MIL-101(Cr)-supported Pt and Co catalysts

A series of MIL-101(Cr)-supported Pt and Co catalysts was prepared by using a simple ethylene glycol (EG) reduction method.³¹ Briefly, MIL-101(Cr) (0.15 g) was put into a mixture of 10 mL EG and 5 mL dimethylformamide (DMF) under stirring for 5 min to obtain mixture A. 1.2 g of a pre-prepared 1 wt% $\text{H}_2\text{PtCl}_6 \cdot 6\text{H}_2\text{O}$ aqueous solution and 0.74 g (2.2 and 3.7 g) of a pre-prepared 1 wt% $\text{Co}(\text{NO}_3)_2 \cdot 6\text{H}_2\text{O}$ aqueous solution were added to 10 mL EG to obtain solution B. Then, solution B was added to mixture A dropwise while continuously stirring at room temperature; this process took about 20 min to complete. The mixture was further stirred for 5 h at room temperature, after which it was treated in an ultrasonic bath for 10 min and then transferred to a stainless steel autoclave coated with a Teflon inner layer. The reduction reaction was performed at 150 °C for 24 h under static conditions. Finally, the resulting catalyst was separated by filtration and washed with ethanol until it was free of Cl^- , as determined by testing with an aqueous AgNO_3 and HNO_3 solution. The catalysts were then dried at 60 °C under vacuum for 12 h. A series of MIL-101(Cr)-supported catalysts were prepared, a monometallic 3%Pt/MIL-101(Cr) and several Pt-Co intermetallic nanoparticle (IMN) catalysts with various 3:y wt% ratios, which we denote here as 3%Pt_yCo/MIL-101(Cr) (y = 1, 3, 5).

2.3. Characterization

The contents of platinum and cobalt in the prepared catalysts were measured by inductively coupled plasma-optical emission spectrometry (ICP-OES), which was performed by using a PerkinElmer Optima 7000DV analyser. Before measurement, each sample was dissolved in *aqua regia* ($\text{HCl} + \text{HNO}_3$). The crystallinity of the samples was assessed *via* X-ray diffraction (XRD) tests, conducted on a Bruker D8 Advance X-ray diffractometer using $\text{Cu K}\alpha$ ($\lambda = 1.5418 \text{ \AA}$) radiation (40 kV, 40 mA); the data were collected in the 5–80° 2θ range. FTIR spectra were obtained by diluting the catalysts in KBr powder and making pellets, using a Bruker Equinox 55 IR spectrometer. N_2 adsorption–desorption isotherms, used to investigate the properties of the porous structures at –196 °C, were measured using a Micromeritics Tristar II surface area and porosity analysis instrument. In each test, the catalyst (more than 100 mg) was preheated under vacuum

at 150 °C for 5 h before measurement (to remove the adsorbed water), and the pore size distribution and surface area were calculated from desorption isotherms by using the Barrett–Joyner–Halenda (BJH) and Brunauer–Emmett–Teller (BET) methods, respectively. The morphology and structure of the catalysts were imaged by scanning electron microscopy (SEM) (Hitachi S-4800) and transmission electron microscopy (TEM) (JEM-2100). The surface composition was analyzed by using X-ray photoelectron spectroscopy (XPS) (Kratos-AXIS ULTRA DLD), employing an Al $\text{K}\alpha$ radiation source. The binding energies (BEs) were calibrated and referenced to the C (1s) binding energy of adventitious carbon, taken to be 284.0 eV. X-ray absorption near-edge structure (XANES) and extended X-ray absorption fine structure (EXAFS) spectra were acquired at the BL14W1 station in the Shanghai Synchrotron Radiation Facility (SSRF, 3.5 GeV, 250 mA). A Si (311) double-crystal monochromator was used to monochromatize the X-ray beam. The surface electronic properties of the Pt metal species were also investigated *via* infrared absorption spectroscopy by using carbon monoxide (CO) as a probe molecule and a Nicolet 6700 FTIR spectrometer. The surface acidity of the catalysts was confirmed by ammonia temperature-programmed desorption (NH_3 -TPD). The results were recorded using an AutoChem TP5080 chemisorption analyser (Xianquan Tianjin China) equipped with a TCD detector, and the ammonia signal ($m/z = 17$) was recorded using mass spectrometry (QIC-20, Hidden).

2.4. Liquid-phase hydrogenation reaction

The liquid-phase selective hydrogenation of CAL and of FFL was performed in a 100 mL stainless steel autoclave. Typically, for each reaction, CAL/FFL (0.2525 g), the catalyst (20.0 mg), and isopropanol (15 mL), used as solvent, were introduced into the stainless steel autoclave fitted with a temperature-controlled furnace. Afterwards, the autoclave was flushed three times with N_2 at 0.5 MPa to displace the air in its volume, and then H_2 (0.5 MPa) was added to replace the N_2 in the reactor, flushing three times to make sure that all of the N_2 was removed. Subsequently, the reactor was filled with hydrogen (pressure 0.6–1.2 MPa) and heated to the required temperature (30–80 °C) under magnetic stirring (800 rpm) for the required time (10–120 min). In the stability and reusability tests, the used catalyst was recovered by centrifugation, washed three times with isopropanol, dried at 60 °C under vacuum, and used for the next run under the same conditions without any further treatment. After reaction, the solution was filtered to screen out the solid catalyst, and the products were analyzed by gas chromatography (BFRL SP-3420, Beijing, China, equipped with a flame ionization detector (FID) and a HP-5 capillary column, 30 m × 0.32 mm × 0.25 μm), using octanol as the external standard.

3. Results and discussion

3.1. Catalyst characterization

3.1.1. Metal loading quantitation. The presence of the encapsulated Pt and Co metal nanoparticles in 3%Pt/MIL-

101(Cr), 3%Pt1%Co/MIL-101(Cr), 3%Pt3%Co/MIL-101(Cr), and 3%Pt5%Co/MIL-101(Cr) was first confirmed by ICP-OES. The results are listed in Table 1 (first two columns). It can be seen here that the actual Pt metal loading attained was in all cases close to, albeit somewhat lower than, the 3 wt% target. The added Co also amounted to values close to those planned for, although the Co:Pt wt% γ :3 ratios were in all cases a little below the targeted numbers.

3.1.2. Bulk structure analysis. Fig. 1 shows the XRD patterns obtained for the synthesized pure MIL-101(Cr), for 3%Pt/MIL-101(Cr), and for three 3%Pt γ %Co/MIL-101(Cr) catalysts ($\gamma = 1, 3, 5$). By and large, they all show the same diffraction peaks, an observation in good agreement with the results of MIL-101(Cr) reported in the literature.^{37,38,46} Specifically, peaks are seen in all cases at $2\theta = 5.2^\circ, 9^\circ$ and 16.6° . This demonstrates that the crystal structure of the pristine MIL-101(Cr) is retained upon loading of the Pt and Co nanoparticles. Moreover, no obvious diffraction peaks assignable to the Pt or Co species (expected at values of $2\theta = 39.7^\circ$) are observed in any of the 3%Pt/MIL-101(Cr) or 3%Pt γ %Co/MIL-101(Cr) samples, suggesting that the Pt and Pt-Co intermetallic nanoparticles (IMNs) are quite small and well dispersed inside the pores of the MIL-101(Cr) support. Nevertheless, the intensity of the diffraction peaks from the support become partially suppressed after the addition of the Pt and Co nanoparticles, indicating a slight decrease in the mesoporous ordering of the pristine MIL-101(Cr). Moreover, there are minor differences in some of the X-ray diffraction patterns, in particular in those for the 3%Pt1%Co/MIL-101(Cr) and 3%Pt5%Co/MIL-101(Cr) samples, as compared to the 3%Pt3%Co/MIL-101(Cr) sample. Extra diffraction peaks at 2θ of $12.2^\circ, 24.6^\circ, 62.5^\circ$ and 66° are observed for the 3%Pt1%Co/MIL-101(Cr) and 3%Pt5%Co/MIL-101(Cr) samples that cannot be matched with any phases by searching the PDF database using XRD Analysis Software (Jade 5.0) and the literature. We think extra diffraction peaks may be assigned because the MOF structure is destroyed to some extent in the hydrothermal reduction of Pt species using ethylene glycol as a reductant. No such peaks are seen in the XRD pattern of 3%Pt3%Co/MIL-101(Cr), indicating a more uniform distribution of Pt-Co IMNs confined within MIL-101(Cr).^{36,38,40}

To further characterize the structure of the MIL-101(Cr), 3%Pt/MIL-101(Cr), and 3%Pt γ %Co/MIL-101(Cr) catalysts ($\gamma = 1, 3, 5$), their FTIR spectra were acquired (Fig. S1†). All the Pt/Pt-Co supported MIL-101(Cr) catalysts exhibit similar IR

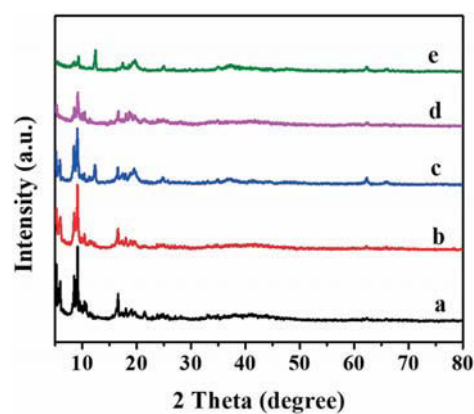


Fig. 1 XRD spectra of (a) MIL-101(Cr), (b) 3%Pt/MIL-101(Cr), (c) 3%Pt1%Co/MIL-101(Cr), (d) 3%Pt3%Co/MIL-101(Cr), and (e) 3%Pt5%Co/MIL-101(Cr).

spectra. Absorption bands are seen at 1400 and 1624 cm^{-1} for all the samples, attributed to the asymmetric and symmetric stretching vibrations of the carboxyl (COO^-) groups of the terephthalic acid (H_2BDC) present in the MIL-101(Cr) framework, respectively.⁴⁶ Additional weak and narrow bands were detected at $749, 1017$ and 1160 cm^{-1} , ascribed to $\delta(\text{C-H})$ and (two) $\gamma(\text{C-H})$ vibrations of the aromatic rings, respectively. The weak band at 580 cm^{-1} can be attributed to the in-plane and out-of-plane bending modes of the COO^- groups, and the intense and broad bands around 3434 cm^{-1} can be assigned to the O-H stretching vibrations, suggesting the presence of water molecules within the catalysts.⁴⁶ The detection of all major vibrational modes for the organic linkers in our MOF confirms that the host MIL-101(Cr) structure is retained after the loading of the Pt/Pt-Co IMNs, in agreement with the XRD results (Fig. 1).

3.1.3. Pore structure characterization. The surface areas and pore volumes of the synthesized samples were determined by N_2 adsorption-desorption isotherm measurements; the results are summarized in Fig. 2 and Table 1. As shown in Fig. 2, the N_2 adsorption-desorption isotherms of MIL-101(Cr), 3%Pt/MIL-101(Cr) and 3%Pt γ %Co/MIL-101(Cr) all show a combination of type I and type IV curves, according to the IUPAC classification, characteristic of materials containing both micropores and mesopores.⁴⁰ The BET surface area and total pore volume of the pristine MIL-101(Cr) were estimated by the BJH method to be $2674\text{ m}^2\text{ g}^{-1}$ and $1.40\text{ cm}^3\text{ g}^{-1}$,

Table 1 Physicochemical parameters of the catalysts made in this study

Catalysts	Pt loading (wt%)	Co loading (wt%)	Lewis acidity (mmol g^{-1})	BET surface area ($\text{m}^2\text{ g}^{-1}$)	Pore volume ($\text{cm}^3\text{ g}^{-1}$)	Content of Pt species (%)		
						Pt ⁰	Pt ²⁺	Pt ⁴⁺
MIL-101(Cr)	—	—	0.40	2674	1.40	—	—	—
3%Pt/MIL-101(Cr)	2.74	—	0.47	2588	1.08	46	19	35
3%Pt1%Co/MIL-101(Cr)	2.83	0.90	0.73	2296	1.28	45	21	34
3%Pt3%Co/MIL-101(Cr)	2.89	2.87	0.78	1930	1.18	47	15	38
3%Pt5%Co/MIL-101(Cr)	2.85	4.61	0.80	1416	1.01	42	10	48
Used 3%Pt3%Co/MIL-101(Cr)	—	—	—	2069	1.28	55	18	27

respectively. Both of these parameters decrease to $2588 \text{ m}^2 \text{ g}^{-1}$ and $1.08 \text{ cm}^3 \text{ g}^{-1}$, respectively, upon the addition of 3 wt% Pt, and go down further with increasing Co content (with the exception of the volume for the pure Pt sample that seems to be lower than expected). The significant decrease in the values of these physical parameters is likely the result of pore blocking by the Pt and Co IMPs. Nevertheless, all the catalysts exhibit similar pore size distributions, centered around $\sim 2.3 \text{ nm}$, as indicated in Fig. 2b (except for 3%Pt5%Co/MIL-101(Cr), which shows pore diameters centered around $\sim 2.0 \text{ nm}$). Combined with the XRD results, we think the pore structure changes can be assigned to the partially broken metal–organic framework to some extent after Pt and Co addition, especially for 3%Pt5%Co/MIL-101(Cr).

3.1.4. SEM and TEM imaging. The morphology of the as-synthesized 3%Pt/MIL-101(Cr) and 3%Pt γ %Co/MIL-101(Cr) catalysts were characterized by SEM. Typical images are shown in Fig. 3. They reveal that 3%Pt/MIL-101(Cr) (Fig. 3a) possesses a similar morphology to MIL-101(Cr) (Fig. S2 \dagger): both exhibit regular well-defined octahedral shapes with clear edges and corners, consistent with previous reports.^{34,39} However, it is clear from the images in Fig. 3b–d that the surface morphology becomes slightly rougher with the addition of Co.

Higher resolution TEM images are shown in Fig. 4. They indicate that the Pt and Pt–Co IMPs are uniformly distributed throughout the support, mostly confined inside the pores of the MIL-101(Cr) support; no nanoparticle aggregation or their presence on the outer surface of MIL-101(Cr) is apparent. The average nanoparticle sizes (d) estimated from these images are all similar, around $d = 2.1 \pm 0.45 \text{ nm}$, but perhaps increase slightly with increasing Co content ($d = 2.1 \pm 0.5$, 2.3 ± 0.5 , and $2.3 \pm 0.4 \text{ nm}$ for 3%Pt1%Co/MIL-101(Cr), 3%Pt3%Co/MIL-101(Cr) and 3%Pt5%Co/MIL-101(Cr), respectively; Fig. 4). This trend is to be expected, as the total metal content increases with increasing Co load (the Pt wt% is approximately the same in all cases, Table 1).

The crystal structure of the Pt–Co IMNs in 3%Pt3%Co/MIL-101(Cr) and their uniform dispersion were confirmed by

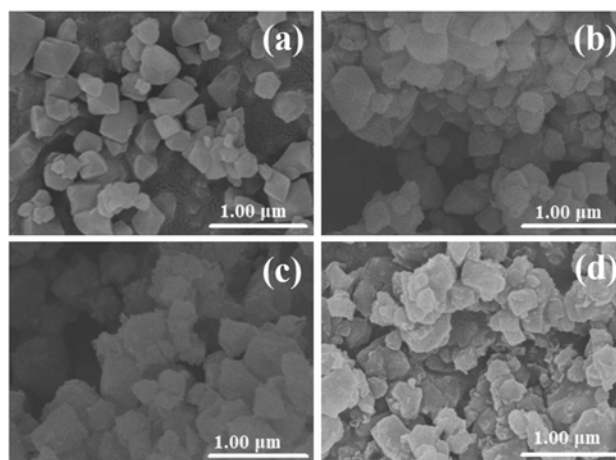


Fig. 3 SEM images of (a) 3%Pt/MIL-101(Cr), (b) 3%Pt1%Co/MIL-101(Cr), (c) 3%Pt3%Co/MIL-101(Cr) and (d) 3%Pt5%Co/MIL-101(Cr).

HRTEM and by the corresponding element maps, shown in Fig. 4d and e, respectively. In Fig. 4d, crystal fringes are observed with calculated d -spacings of 0.229 and 0.225 nm, which are assigned to the (111) plane of the face-centred cubic Pt and Pt–Co crystals, respectively.^{24,47} Fig. 4e also shows the uniform nature of the dispersion of both Pt and Co metals. This TEM analysis suggests that small-sized uniformly dispersed Pt–Co IMNs confined within the pores of MIL-101(Cr) can be prepared by the polyol reduction method. It would also appear that the large surface area and high porosity of MIL-101(Cr) are beneficial for the uniform dispersion of Pt–Co IMNs.

3.1.5. Analysis of surface species. To study the surface electronic states of the Pt species and the interaction between Pt and Co in the Pt–Co IMNs, the 3%Pt/MIL-101(Cr), 3%Pt1%Co/MIL-101(Cr), 3%Pt3%Co/MIL-101(Cr) and 3%Pt5%Co/MIL-101(Cr) samples were probed by XPS. Survey XPS spectra are provided in Fig. S3 \dagger and the Pt 4f spectra, deconvoluted into the different valence states by fitting

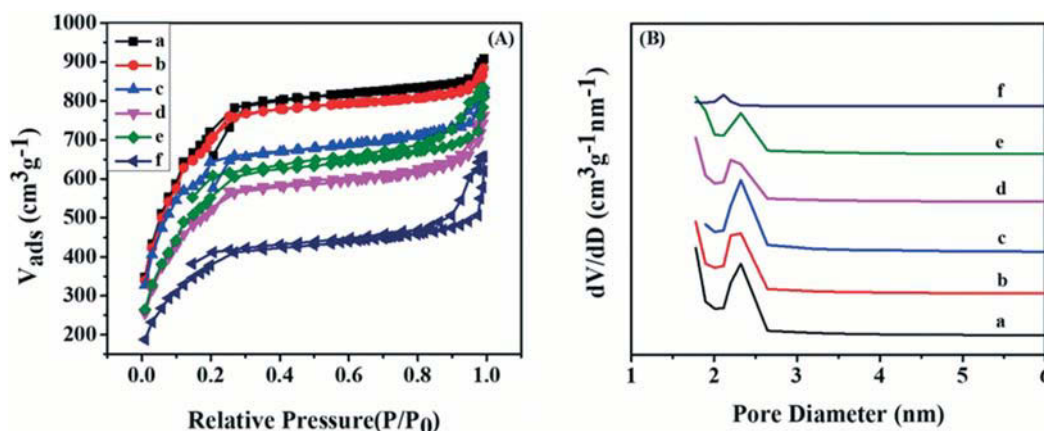


Fig. 2 (A) N_2 -adsorption-desorption isotherms and (B) pore size distributions for (a) MIL-101(Cr), (b) 3%Pt/MIL-101(Cr), (c) 3%Pt1%Co/MIL-101(Cr), (d) 3%Pt3%Co/MIL-101(Cr), (e) used-3%Pt3%Co/MIL-101(Cr) and (f) 3%Pt5%Co/MIL-101(Cr).

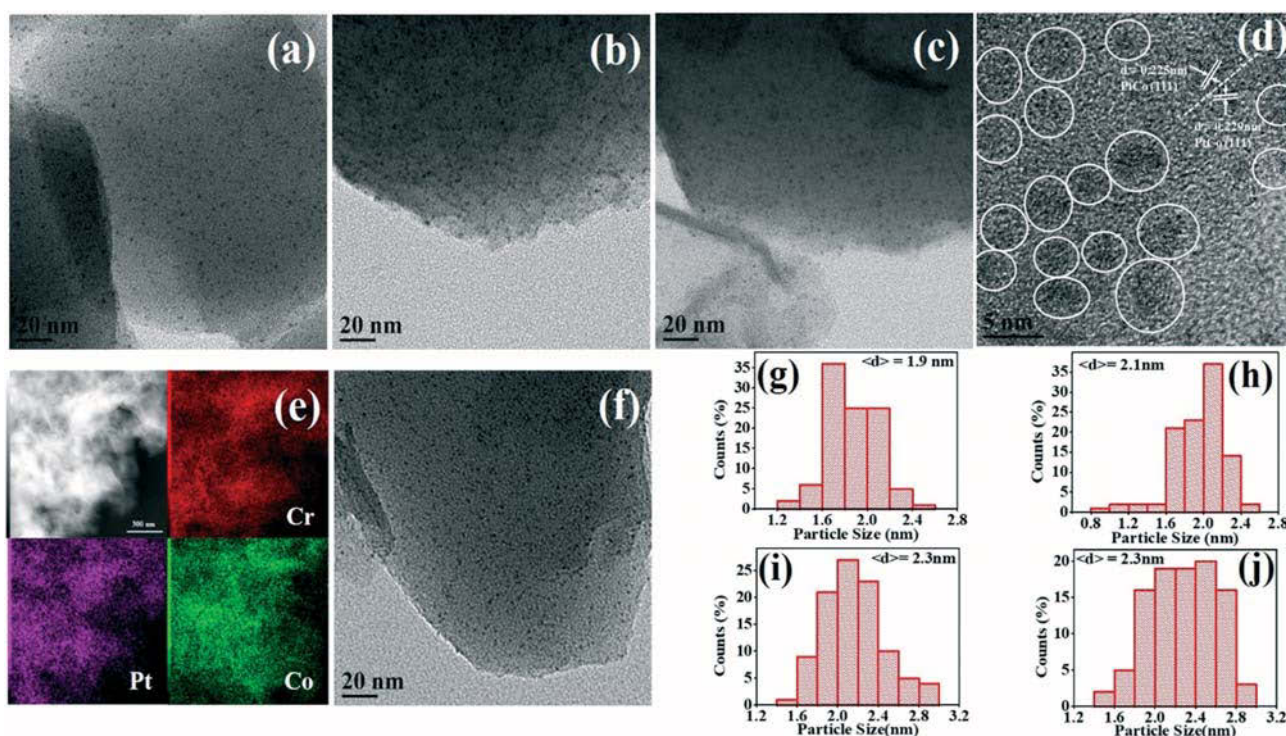


Fig. 4 (a) TEM image and (g) particle size distribution for 3%Pt/MIL-101(Cr); (b) TEM image and (h) particle size distribution for 3%Pt1%Co/MIL-101(Cr); (c) TEM image, (d) HETEM image, (e) element maps (scale = 300 nm) and (i) particle size distribution for 3%Pt3%Co/MIL-101(Cr); (f) TEM image and (j) particle size distribution for 3%Pt5%Co/MIL-101(Cr).

Gaussian peaks after Shirley-background subtraction (and by fixing the peak separation and area ratios between the $4f_{7/2}$ and $4f_{5/2}$ peaks due to spin splitting), are shown in Fig. 5 (the resulting Pt $4f_{7/2}$ peak positions are shown in Table S1†). According to previous literature,^{2,24,48} binding energies (BEs) for the Pt $4f_{7/2}$ feature at 70.8–71.4 eV, 73.5–73.7 eV, and 75.5–75.7 eV are characteristic of zero-valent metallic Pt (Pt^0) and oxidized Pt^{2+} and Pt^{4+} species, respectively.

The percentages of Pt^0 , Pt^{2+} , and Pt^{4+} surface species in the samples calculated from these data are summarized in Table 1. In general, the percentage of metallic Pt^0 remains approximately constant (within experimental error) with increasing Co content; values between 42% and 47% were measured for all 3%Pt/MIL-101(Cr), 3%Pt1%Co/MIL-101(Cr), 3%Pt3%Co/MIL-101(Cr) and 3%Pt5%Co/MIL-101(Cr). On the other hand, the fraction of Pt^{4+} increases with Co content, at the expense of the amount of Pt^{2+} . It would seem that the presence of Co facilitates the deep oxidation of Pt atoms. It should be noted, though, that these distributions of Pt oxidation states correspond to the as-synthesized samples; they are expected to change upon preconditioning of the catalysts and after their use for the promotion of hydrogenation reactions (which are carried out in a strongly reducing environment) (more on this below). Also noteworthy is that the position of the Pt^0 XPS peak blue-shifts significantly upon the addition of Co atoms to the IMNs (BE($\text{Pt}^0 4f_{7/2}$) = 70.8 eV vs. 71.35 eV for the 3%Pt/MIL-101(Cr) vs. 3%Pt1%Co/MIL-101(Cr) samples, respectively; Table S1†).

This suggests that there is a significant net charge transfer from Pt to Co in the bimetallic IMPs. The effect reverses somewhat upon further addition of Co (BE($\text{Pt}^0 4f_{7/2}$) = 71.15 eV and 71.05 eV for 3%Pt3%Co/MIL-101(Cr) and 3%Pt5%Co/MIL-101(Cr), respectively), possibly because of charge saturation of the Co centers. Perhaps the important observation here is that the electronic properties of the metallic Pt atoms can be fine-tuned *via* the controlled addition of Co.

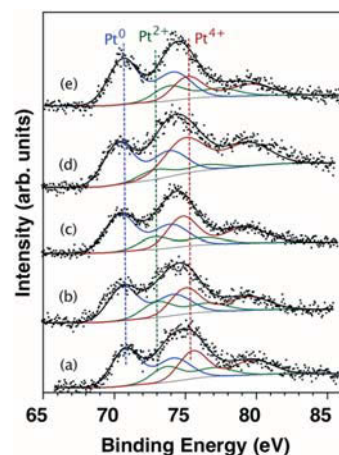


Fig. 5 Pt 4f XPS spectra of (a) 3%Pt/MIL-101(Cr), (b) 3%Pt1%Co/MIL-101(Cr), (c) 3%Pt3%Co/MIL-101(Cr), (d) 3%Pt5%Co/MIL-101(Cr), and (e) used 3%Pt3%Co/MIL-101(Cr).

The corresponding Co 2p XPS data are shown in Fig. S4.† It is seen there that the Co species are typically in an oxidized state on the surface as Co^{2+} and Co^{3+} rather than Co^0 .⁴⁸ Unfortunately, given the low signal-to-noise ratio of the spectra, it is not possible to reliably deconvolve these spectra into their Co^{2+} and Co^{3+} constituents, and therefore no quantitative analysis can be provided (a tentative set of fitted curves is shown in Fig. S4†). However, the data confirm that the cobalt species are in a partially charged state ($\text{Co}^{\delta+}$) and that they are more oxidized (there are larger components in the spectra for the higher Co oxidation states) in the samples with higher Co content. This parallels the trend seen with Pt. However, as discussed above, the presence of oxidized CoO_x surface species because of exposure of the catalysts to air cannot be ruled out; these data are not representative of the nature of the working catalyst and can only be used to extract general trends in terms of ease of oxidation and charge transfer.

3.1.6. CO-FTIR and NH_3 -TPD titration of surface sites. The surface electronic properties of the Pt surface species were also investigated by characterizing the adsorption of carbon monoxide, a molecule often used as a probe, using *in situ* FTIR spectroscopy (Fig. S5 and Table S2†). As expected, no band for the linear adsorption of CO atop Pt metal sites, expected between 2000 and 2090 cm^{-1} , was observed for the pristine MIL-101(Cr).¹⁰ Instead, two weak bands are evident between 2100 and 2200 cm^{-1} , assigned to the physisorption of gaseous CO molecules.³⁶ In contrast, atop CO adsorption is clearly evident in the spectra with metal nanoparticles. On 3%Pt/MIL-101(Cr), the C–O stretching vibration of that species is seen at 2068 cm^{-1} . Interestingly, the IR peak red shifts slightly upon the addition of Co, although the effect is quite subtle and not fully consistent: no variations larger than 10 cm^{-1} are seen, and the sample with the largest Co content shows a reverse in this trend (Table S2†). This result is at first sight difficult to square with the XPS results, because a C–O stretching frequency red shift implies an increase in electron density in the d orbitals that participate in the π^* C=O bond. However, it should be noted that the electron transfer in IMPs tends to involve mainly the delocalized sp electronic band, not these localized d

orbitals. Clearly, the picture on the modification of the electronic properties of Pt upon the addition of Co is nuanced and complex. Nevertheless, it is important in terms of the tuning of catalytic properties.^{10,49}

NH_3 -TPD experiments were also carried out to characterize any potential acidic sites on the surface of the catalysts. The data are reported in Fig. S6.† In that figure, the appearance of broad features in the 150–390 °C range can be assigned to desorption of NH_3 bonded to the open Cr^{3+} Lewis acid sites, confirming the presence of moderate Lewis acid sites.³⁶ In terms of the quantitation of those sites, Table 1 indicates that the coverage of Lewis acids increases significantly with Co addition, going from 0.40 mmol g^{-1} on the pure support to 0.73 mmol g^{-1} for 3%Pt1%Co/MIL-101(Cr). However, the Lewis acid amount only increases to 0.80 mmol g^{-1} as the Co content is 5%, which can be ascribed to the significant decrease in the specific surface area from 2296 $\text{m}^2 \text{g}^{-1}$ for 3%Pt1%Co/MIL-101(Cr) to 1416 $\text{m}^2 \text{g}^{-1}$ for 3%Pt5%Co/MIL-101(Cr) (Table 1). The shape of the desorption traces also becomes more complex, indicating the presence of new adsorption sites. It is quite possible that in addition to the Lewis sites of the support, new adsorption sites are generated at either the IMPs or, perhaps more likely, at the interface between the metal nanoparticles and the support. Because the ammonia uptake increases with Co content, it appears that it is the Co species that participate in this new ammonia adsorption.

3.1.7. XANES and EXAFS results. The electronic structure and local coordination of the Pt species in 3%Pt/MIL-101(Cr) and 3%Pt3%Co/MIL-101(Cr) were also examined by XANES and EXAFS. Representative data are shown in Fig. 6. As seen from the normalized Pt L_3 -edge XANES curves shown in Fig. 6A, the 3%Pt/MIL-101(Cr) and 3%Pt3%Co/MIL-101(Cr) samples show identical absorption threshold energies and peak shapes, starting at higher energies than that seen in the reference data obtained for a Pt metal foil. This indicates the presence of some of the Pt in oxidized form ($\text{Pt}^{\delta+}$ species), in agreement with the XPS results (Fig. 5).

Fig. 6B shows the radial distributions calculated from analysis of the EXAFS data. They reveal the presence of not

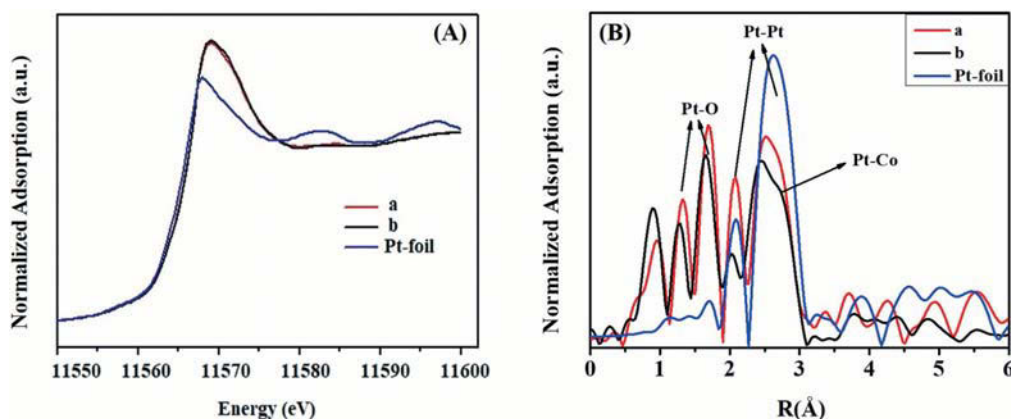


Fig. 6 (A) Normalized XANES spectra at the Pt L_3 -edge of (a) 3%Pt/MIL-101(Cr) and (b) 3%Pt3%Co/MIL-101(Cr). (B) Radial distributions calculated from EXAFS data for (a) 3%Pt/MIL-101(Cr) and (b) 3%Pt3%Co/MIL-101(Cr).

only Pt–Pt bonds (Pt^0 species; $R_{\text{Pt-Pt}}$ 2.74 \pm 0.01 and 2.73 \pm 0.01 Å for 3%Pt/MIL-101(Cr) and 3%Pt3%Co/MIL-101(Cr), respectively) but also Pt–O bonds (Pt^{O^+} species, $R_{\text{Pt-O}}$ = 2.00 \pm 0.02 Å and 1.98 \pm 0.02 Å); this is the case in both 3%Pt/MIL-101(Cr) and 3%Pt3%Co/MIL-101(Cr) samples. The Pt–Pt bonds seem to be slightly shorter than those in the reference Pt foil, and the coordination numbers much smaller, likely a reflection of the small size of the IMNs. Furthermore, a small shoulder peak at 2.7 Å confirms the formation of Pt–Co IMNs.^{50–52} In addition, the coordination number (CN) may also be employed to recognize the formation and existence of the Pt–Co bond. As shown in Table S3,† the CN values for 3%Pt/MIL-101(Cr) and 3%Pt3%Co/MIL-101(Cr) are much smaller than those in the reference Pt-foil, confirming the formation of the Pt–Pt bond. Moreover, the CN value (for the Pt–Pt bond) for the 3%Pt3%Co/MIL-101(Cr) sample is higher than that for the 3%Pt/MIL-101(Cr) sample. Also, the CN value for the Pt–O bond is less for 3%Pt3%Co/MIL-101(Cr) compared with the 3%Pt/MIL-101(Cr) sample, suggesting that Pt is more reduced in the 3%Pt3%Co/MIL-101(Cr) sample (consistent with XPS results).

3.2. Catalytic activity results

3.2.1. Activity over 3%Pt y %Co/MIL-101(Cr). The selective hydrogenation of CAL to produce COL was chosen as a model reaction to evaluate the catalytic performance of our different 3%Pt y %Co/MIL-101(Cr) catalysts. In Table 2, we report the basic kinetic results from such study. The blank kinetic run, without a catalyst, resulted in almost no conversion of CAL (data not shown), a result that not only highlights the role of the catalyst but also confirms that transfer hydrogenation is insignificant under our reaction conditions. One conclusion from the data in Table 2 is that the catalytic performance is significantly influenced by the introduction of Co in the 3%Pt y %Co/MIL-101(Cr) catalysts. Indeed, while the 3%Pt/MIL-101(Cr) catalyst yields a 53% conversion of CAL with 20% selectivity toward COL after 5 h under 1 MPa hydrogen and at 60 °C, those numbers increase significantly, to 73% and 86%, respectively, after only 2 h with the 3%Pt1%Co/MIL-101(Cr) catalyst, and to 95% and 91% in 2 h over 3%Pt3%Co/MIL-101(Cr) (under similar reaction conditions). The 3%Pt3%Co/MIL-101(Cr) catalyst reaches the optimum performance as the activity declines to 67% and the

selectivity to 89% over 3%Pt5%Co/MIL-101(Cr). Similar trends were seen for the hydrogenation of FFL: as listed in Table 2, a 97% conversion with a 94% selectivity to FOL was seen with 3%Pt3%Co/MIL-101(Cr), much higher values than those measured with the other catalysts.

Based on the above results, it can be concluded that the best catalyst in our set for selective hydrogenation is 3%Pt3%Co/MIL-101(Cr). Accordingly, we chose to perform more detailed kinetic measurements for the selective hydrogenation of CAL and FFL with that sample.

3.2.2. Effect of reaction time. The hydrogenation of both CAL and FFL was followed as a function of reaction time by sampling and analyzing the reaction mixtures after 10, 15, 20, 25 and 30 min of the start of the conversion using the 3%Pt3%Co/MIL-101(Cr) catalyst. These experiments were performed at different temperatures, at 30, 45, 60, 70 and 80 °C, as discussed in the next section. As can be seen in Fig. S7–S9,† the primary selectivity towards the unsaturated alcohols (COL and FOL, respectively) is higher than those of any of the other products at all times and temperatures. Examples of the kinetic data acquired in these runs over a longer time period (several hours) is provided in Fig. 7 for the hydrogenation of both CAL and FFL at 60 °C. It is seen there that total conversion of both CAL and FFL is reached within 3 h, slightly faster with FFL, and that the initial selectivity toward the unsaturated alcohols (COL and FOL) is about 90%. The selectivities toward COL (Fig. 7A) and FOL (Fig. 7B) are quite high at all times, starting above 90%, but decrease slightly with time because of the subsequent hydrogenation of those primary products to the saturated alcohols, as indicated in Scheme 1.

In the case of CAL, the hydrogenation of COL to the corresponding saturated alcohol (hydrocinnamyl alcohol, HCOL) is much easier than in the case of the secondary hydrogenation of the FOL produced *via* hydrogenation of FFL (Fig. 7), which indicates that FOL is more stable than COL under our reaction conditions. A 2 h reaction time was selected for the subsequent studies to minimize the effect of this secondary reaction. Critically, no significant amounts of the saturated aldehyde, the competing primary product, were detected at any time during the course of these reactions.

3.2.3. Effect of reaction temperature over 3%Pt3%Co/MIL-101(Cr). The effect of reaction temperature on the CAL and FFL hydrogenation was investigated in the 30–80 °C range under a 1

Table 2 Catalytic performance of our catalysts for the conversion of CAL and FFL

Catalyst	CAL conversion (%)	Selectivity (%)				FFL conversion (%)	FOL selectivity (%)	TOF ^e (h ⁻¹)
		COL	HCOL	HCOL	Others			
3%Pt/MIL-101(Cr)	53 ^a	20	59	15	6	37 ^c	66	111
3%Pt1%Co/MIL-101(Cr)	73 ^b	86	5	8	1	69 ^d	83	397
3%Pt3%Co/MIL-101(Cr)	95 ^b	91	6	2	1	97 ^d	94	546
3%Pt5%Co/MIL-101(Cr)	67 ^b	89	3	2	7	69 ^d	90	377

Reaction conditions: 60 °C, 1 MPa H₂ pressure, 0.2525 g CAL^{a,b}/FFL^{c,d}, 20 mg catalyst, 15 mL isopropanol. ^a 5 h reaction times. ^b 2 h reaction times. ^c 3 h reaction times. ^d 2 h reaction times. ^e TOF = [moles of COL yield]/[(moles of Pt loading) × (reaction time) × (% dispersion/molecular weight of Pt)].

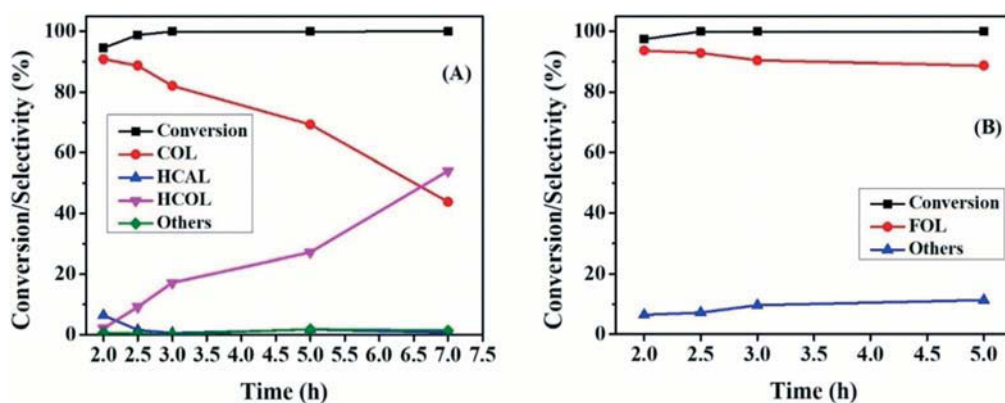


Fig. 7 Selective hydrogenation of (A) CAL and (B) FFL as a function of reaction time over the 3%Pt3%Co/MIL-101(Cr) catalyst (reaction conditions: 60 °C, 1 MPa H₂ pressure, 0.2525 g CAL, 0.2525 g FFL, 20 mg catalysts, 15 mL isopropanol, 800 rpm).

MPa H₂ pressure. The results, presented in Fig. 8, indicate the excellent catalytic activity of 3%Pt3%Co/MIL-101(Cr) in this entire temperature range, even at room temperature (30 °C). As expected, increasing the reaction temperature leads to an increase in CAL (Fig. 8A) and FFL (Fig. 8B) conversions (in this case reported for a fixed 2 h reaction time), as in any activated reaction. Importantly, the selectivity toward the desired

unsaturated alcohols, *i.e.*, toward COL and FOL, is >90% in the whole 30–60 °C range. That selectivity declines slightly at the higher reaction temperatures (70 and 80 °C), but such a trend can again be explained by an enhancement in the further hydrogenation of the primary products, as discussed above.

Additional time-dependent kinetic studies were performed for the CAL hydrogenation at five different

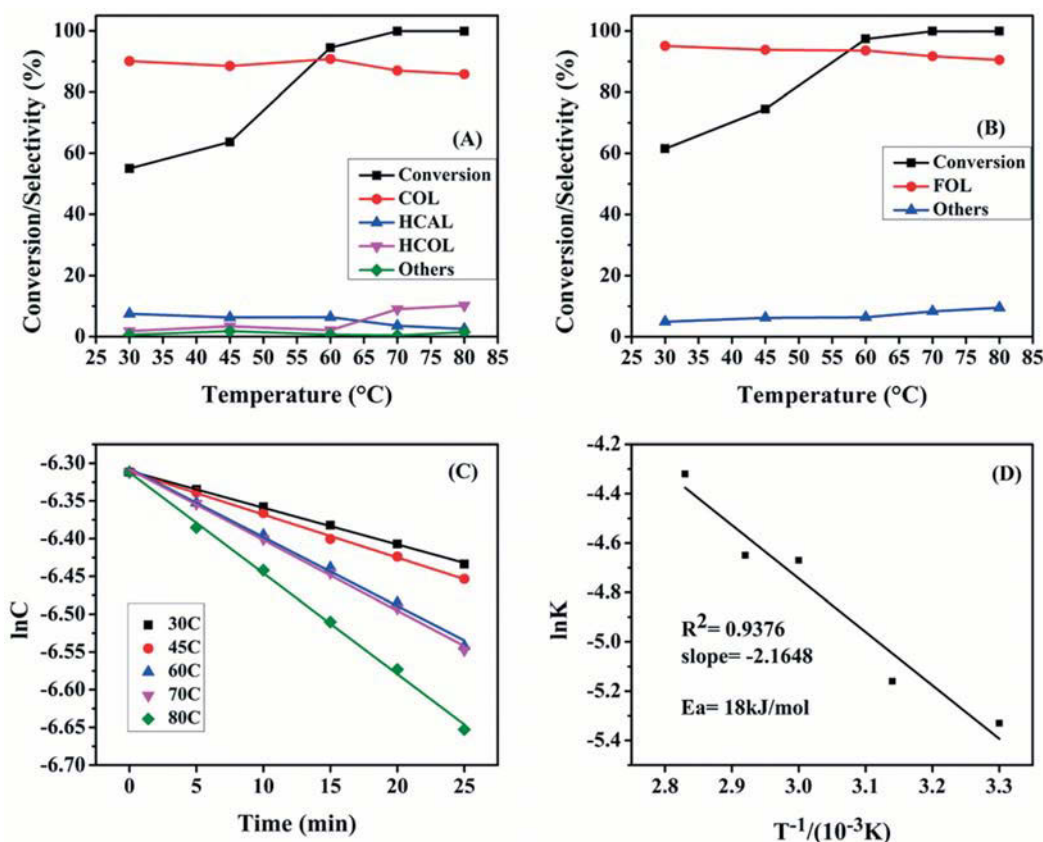


Fig. 8 Conversion and selectivity after 2 h for the hydrogenation of (A) CAL and (B) FFL vs. temperature over 3%Pt3%Co/MIL-101(Cr). (C) Plot of $\ln C$ vs. time for the conversion of CAL at different temperatures. (D) Arrhenius plot of the first-order rate constants extracted from the data shown in (C).

temperatures *i.e.* 30, 45, 60, 70 and 80 °C, the results of which are shown in Fig. 8C and S7.† As seen in Fig. 8C, semilogarithmic plots of the percentage of conversion *versus* time show good linear relationships, a hallmark of first-order kinetics. This is in agreement with past literature reports.^{3,40} Subsequent analysis of the resulting reaction rate constants (k), which are plotted in an Arrhenius form ($\ln(k)$ *versus* $1/T$) in Fig. 8D, yielded a value for the apparent activation energy (E_a) of 18 kJ mol⁻¹. There are very limited studies on the estimation of E_a for the hydrogenation of CAL to use a reference: our value, obtained with the 3%Pt3%Co/MIL-101(Cr) catalyst, is comparatively lower than that for 1.5% Pd-WN/SBA-15 (23.2 kJ mol⁻¹), Pt/BN (35 kJ mol⁻¹), Pt/MIL-101 (42.8 kJ mol⁻¹), or Pd-0.3Ag/MCM-41 (75 kJ mol⁻¹).^{3,32,40,53} It would appear that the addition of Co in 3%Pt3%Co/MIL-101(Cr) can reduce the activation energy barrier for the CAL hydrogenation reaction.

3.2.4. Effect of hydrogen pressure. The effect of H₂ partial pressure was also investigated: the H₂ pressure was varied from 0.6 MPa to 1.2 MPa in kinetic studies of the hydrogenation of both CAL and FFL with 3%Pt3%Co/MIL-101(Cr) at relatively low temperatures. It was found that the overall conversion of both CAL and FFL is linearly enhanced with increases in the H₂ partial pressure at both 30 (Fig. S11B and S10B†) and 60 °C (Fig. 9), while the selectivity toward COL and FOL is maintained above 90%. In the case of the CAL hydrogenation, the selectivity toward HCOL is also enhanced slightly at higher H₂ partial pressures (1.2 MPa at 60 °C, Fig. 9A), pointing to the limitation of using high pressures to enhance activity in these reactions. Luckily, the 3%Pt3%Co/MIL-101(Cr) catalyst shows acceptable activity and excellent selectivity for CAL and FFL hydrogenation to the corresponding unsaturated alcohols (COL and FOL) under mild reaction conditions such as 1 MPa H₂ pressure and 60 °C. Table S4† provides data for other Pt-based bimetallic (or IMN) catalysts used in the past for CAL selective hydrogenation for comparison: the catalytic performance of our 3%Pt3%Co/MIL-101(Cr) is comparable to or better than most of those other examples.

3.2.5. Reusability and recyclability of 3%Pt3%Co/MIL-101(Cr). One of the most important concerns with heterogeneous catalysts is their stability and reusability. To assess this issue, recycling experiments were carried out for the hydrogenation of CAL over 3%Pt3%Co/MIL-101(Cr) at 60 °C and 1 MPa H₂. The data are shown in Fig. 10. No appreciable loss in activity or selectivity was seen after up to five runs (the conversion decreased slightly in the fifth run). Further characterization by XPS of the 3%Pt3%Co/MIL-101(Cr) after five cycles indicated a significant increase in the fraction of metallic Pt⁰ on the surface of the IMNs (from 47% to 55%; data for used 3%Pt3%Co/MIL-101(Cr), Fig. 5 and Table 1), a result that is easily understood by the fact that the reaction conditions are highly reducing. The large percentage of Pt that is in a reduced state under the reaction conditions suggests that metallic Pt species (Pt⁰) may play a pivotal role in the hydrogenation reaction. This conclusion is tentative, however, as the XPS analysis was carried out *ex situ*; exposure of the catalyst to ambient conditions after reaction can affect these results.

3.3. Relationship between structure and catalytic performance

The hydrogenation of α,β -unsaturated aldehydes, *i.e.* CAL and FFL, was carried out in the liquid phase for the optimization of the performance of HF-free MIL-101(Cr)-supported Pt/Pt-Co IMN catalysts. As described above, selectivity toward COL is poor when using the monometallic 3%Pt/MIL-101(Cr) catalyst, but it is significantly enhanced, to above 90%, over the 3%PtCo/MIL-101(Cr) catalysts (Table 2). These changes in catalytic performance can be related to the nature of the surface Pt species as they are modified by the addition of Co as well as to the special structure of the MIL-101(Cr) support. The various characterization results indicated the formation of well-mixed and well-dispersed Pt-Co IMNs. Moreover, a strong synergistic effect was identified on the MIL-101(Cr)-based catalysts between the two metals, resulting in a net charge transfer, the extent of which can be tuned by tuning the Pt:Co ratio.

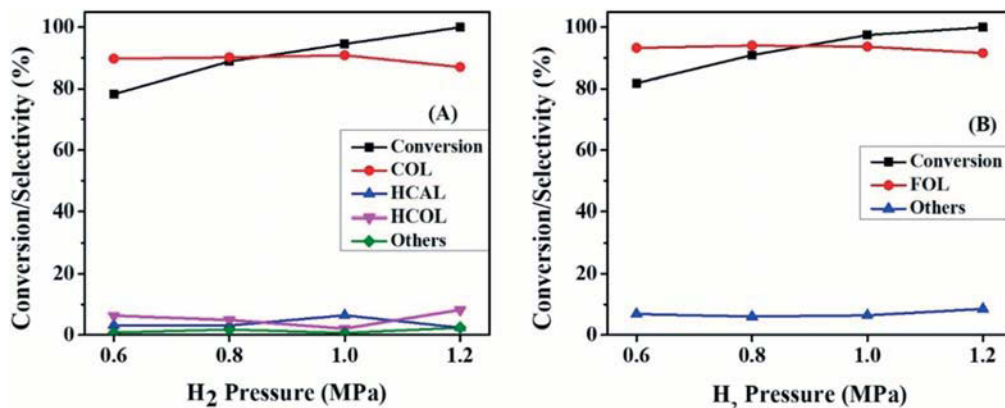


Fig. 9 Selective hydrogenation of (A) CAL and (B) FFL over 3%Pt3%Co/MIL-101(Cr) vs. H₂ pressure. Reaction conditions: 60 °C, 0.2525 g CAL, 0.2525 g FFL, 20 mg catalysts, 15 mL isopropanol, 2 h, 800 rpm.

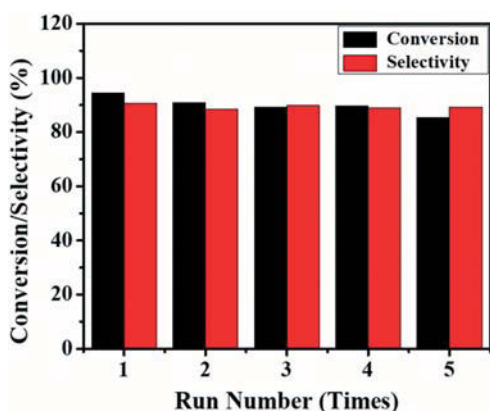


Fig. 10 CAL hydrogenation performance vs. recycling run number with 3%Pt3%Co/MIL-101(Cr) (reaction conditions: 60 °C, 1 MPa H₂ pressure, 0.2525 g CAL, 20 mg catalyst, 15 mL isopropanol, 2 h, 800 rpm).

Generally, in heterogeneous IMN catalyst systems, it has been proposed that electron transfer from the second (electropositive) metal to the first (the main active component) may enhance the catalytic performance of the latter.^{10,13,54,55} As a result, the electron-enriched active metal shows less probability towards C=C bond adsorption (because of d-band electron repulsive forces) and exhibits a decreased heat of adsorption as well as a lower activation barrier for C=O bond activation. These two trends result in the enhanced hydrogenation of the C=O bond.^{56–60} In our specific case, the data reported above from the various characterization studies indicate a strong interaction between Pt and Co atoms in 3%Pt3%Co/MIL-101(Cr). The charge transfer that occurs between the two is, however, somewhat nuanced and difficult to fully understand. On the one hand, the XPS signal for the metallic Pt(0) component shifts toward higher BEs upon the addition of Co, a sign of a loss of electron density. On the other hand, the addition of Co also results in more extensive oxidation (more Pt⁴⁺ formation). There is a minor effect on the strength of adsorption of carbon monoxide as well, as identified by the IR data. In the end, all this characterization was carried out *ex situ*, under conditions much different from those used during catalysis. In fact, the XPS data for the used catalysts showed that much of the initially oxidized Pt becomes reduced after exposure to high H₂ pressures. What is clear is that the addition of Co to Pt does affect its electronic structure (and its ability to be reduced) and that that in turn affects catalytic performance. Although arguments can be put forward about how these charge transfers may favour C=O *versus* C=C adsorption, a more specific model on how that takes place may require electronic characterization of the IMNs *in situ* under reaction conditions.

The other factor that may help with catalytic performance in our samples is the presence of surface Lewis acid, *i.e.*, the Cr³⁺ centers in MIL-101(Cr).^{36,40,61} The Cr³⁺ of MIL-101(Cr) and the electron-modifying Co metal species can act as electrophilic or Lewis acid sites for the adsorption, polarization, and activation of the electron-rich C=O bond (which is a Lewis base) *via* their

lone electron pair at the oxygen atom (electron-donating group). In fact, it is interesting to note that the NH₃-TPD results (Fig. S6† and Table 1) also identify additional base (ammonia) uptake upon the addition of Co to the IMPs, suggesting that new interfacial sites may add to the improved performance of the catalyst. In summary, our 3%Pt3%Co/MIL-101(Cr) catalysts provide both the electronically modified Pt sites and the Lewis acid sites that have been proposed to enhance activity in unsaturated aldehyde hydrogenation reactions. It may also display new IMN-support sites to better direct adsorption and selective reactivity.

Additionally, the metal nanoparticles confined within the narrow pores/channels of the MOF facilitate a strong steric hindrance (steric effect).^{10,45} The Pt–Co IMNs confined within the pores of MIL-101(Cr) generate a strong steric effect and change the adsorption geometry of α,β -unsaturated aldehyde molecules (CAL and FFL) over 3%Pt3%Co/MIL-101(Cr). The α,β -unsaturated aldehyde molecules adsorbed on the surface of Pt–Co IMNs confined within the pores of MIL-101(Cr) vertically *via* the C=O bond end (located at the tail end) while they are sterically hindered the horizontal adsorption *via* the C=C bond end (located in the middle). Thus, the C=O bond reaches the active sites on the catalysts, which is selectively activated and hydrogenated.

Hence, due to the combined synergistic effects of the electronically modified Pt sites and the Lewis acid sites, and the steric effect, the catalytic performance as well as the selectivity toward unsaturated alcohols (COL and FOL) is superior over 3%Pt3%Co/MIL-101(Cr) catalysts (Table 2).

Conclusion

A series of Pt/Pt–Co nanoparticles supported on MIL-101(Cr) (3%Pt/MIL-101(Cr), 3%Pt3%Co/MIL-101(Cr)) were synthesized *via* a polyol reduction method and used to promote the selective hydrogenation of CAL and FFL. It was shown that selectivity toward COL and FOL production can be successfully tuned by designing a homogeneously dispersed Pt–Co intermetallic nanoparticle system confined within the pores of MIL-101(Cr). From the collection of catalysts made here with various Pt:Co content ratios, the 3%Pt3%Co/MIL-101(Cr) catalyst turned out to exhibit the best catalytic performance for the hydrogenation of CAL and FFL, better than that of the rest of the catalysts tried here and also relative to other bimetallic catalysts reported in the literature. CO-FTIR, XPS, XANES, EXAFS and NH₃-TPD studies revealed that Co addition to Pt-based catalysts can help tune the surface electronic structure of the Pt active sites *via* the formation of Pt–Co intermetallic nanoparticles and also enhance the surface Lewis acidity of the catalyst. The formation of additional Lewis acid sites at the MOF–metal interfaces provides a third factor that helps with the improved catalytic performance. The current work opens a new exciting way to attain high selectivity in hydrogenation reactions toward unsaturated alcohols by pairing the use of well-defined supports based on metal organic frameworks

(MIL-101(Cr)) with the dispersion of intermetallic nanoparticles to rely on the synergistic interaction between precious noble metals and other less precious transition metals confined within the pores of MOFs.

Conflicts of interest

The authors declare no competing financial interest.

Acknowledgements

YZ acknowledges the Natural Sciences Fund of Heilongjiang Province (LH2020B021). FZ acknowledges funding from the US National Science Foundation under grant no. CHE-1953843.

References

- L. Zhang, X. Chen, Z. Peng and C. Liang, *Mol. Catal.*, 2018, **449**, 14–24.
- H. Pan, J. Li, J. Lu, G. Wang, W. Xie, P. Wu and X. Li, *J. Catal.*, 2017, **354**, 24–36.
- D. Wang, Y. Zhu, C. Tian, L. Wang, W. Zhou, Y. Dong, H. Yan and H. Fu, *ChemCatChem*, 2016, **8**, 1718–1726.
- Q. Zheng, D. Wang, F. Yuan, Q. Han, Y. Dong, Y. Liu, X. Niu and Y. Zhu, *Catal. Lett.*, 2016, **146**, 1535–1543.
- S. Han, Y. Liu, J. Li, R. Li, F. Yuan and Y. Zhu, *Catalysts*, 2018, **8**, 200.
- D. Wang, Y. Zhu, C. Tian, L. Wang, W. Zhou, Y. Dong, Q. Han, Y. Liu, F. Yuan and H. Fu, *Catal. Sci. Technol.*, 2016, **6**, 2403–2412.
- P. Xiao, J. Zhu, D. Zhao, Z. Zhao, F. Zaera and Y. Zhu, *ACS Appl. Mater. Interfaces*, 2019, **11**, 15517–15527.
- Y. Yang, D. Rao, Y. Chen, S. Dong, B. Wang, X. Zhang and M. Wei, *ACS Catal.*, 2018, **8**, 11749–11760.
- N. Zhang, Q. Shao, P. Wang, X. Zhu and X. Huang, *Small*, 2018, **14**, 1704318.
- X. Lan, K. Xue and T. Wang, *J. Catal.*, 2019, **372**, 49–60.
- M. S. Ide, B. Hao, M. Neurock and R. J. Davis, *ACS Catal.*, 2012, **2**, 671–683.
- O. G. Salnikov, K. V. Kovtunov, D. A. Barskiy, A. K. Khudorozhkov, E. A. Inozemtseva, I. P. Prosvirin, V. I. Bukhtiyarov and I. V. Koptuyug, *ACS Catal.*, 2014, **4**, 2022–2028.
- L.-X. Dai, W. Zhu, M. Lin, Z.-P. Zhang, J. Gu, Y.-H. Wang and Y.-W. Zhang, *Inorg. Chem. Front.*, 2015, **2**, 949–956.
- P. Mäki-Arvela, J. Hájek, T. Salmi and D. Y. Murzin, *Appl. Catal., A*, 2005, **292**, 1–49.
- Y. Ma, G. Xu, H. Wang, Y. Wang, Y. Zhang and Y. Fu, *ACS Catal.*, 2018, **8**, 1268–1277.
- M. Bidaoui, C. Especel, S. Sabour, L. Benatallah, N. Saib-Bouchenafa, S. Royer and O. Mohammedi, *J. Mol. Catal. A: Chem.*, 2015, **399**, 97–105.
- J. P. Stassi, P. D. Zgolicz, S. R. de Miguel and O. A. Scelza, *J. Catal.*, 2013, **306**, 11–29.
- Z. Jiang, W. Wan, Z. Lin, J. Xie and J. G. Chen, *ACS Catal.*, 2017, **7**, 5758–5765.
- B. Seemala, C. M. Cai, C. E. Wyman and P. Christopher, *ACS Catal.*, 2017, **7**, 4070–4082.
- L. Yang, Z. Jiang, G. Fan and F. Li, *Catal. Sci. Technol.*, 2014, **4**, 1123.
- C. Li, Y. Chen, S. Zhang, J. Zhou, F. Wang, S. He, M. Wei, D. G. Evans and X. Duan, *ChemCatChem*, 2014, **6**, 824–831.
- Z. Guo, Y. Chen, L. Li, X. Wang, G. L. Haller and Y. Yang, *J. Catal.*, 2010, **276**, 314–326.
- I. Ro, I. B. Aragao, Z. J. Brentzel, Y. Liu, K. R. Rivera-Dones, M. R. Ball, D. Zanchet, G. W. Huber and J. A. Dumesic, *Appl. Catal., B*, 2018, **231**, 182–190.
- X. Wang, Y. He, Y. Liu, J. Park and X. Liang, *J. Catal.*, 2018, **366**, 61–69.
- B. Li and H. C. Zeng, *ACS Appl. Mater. Interfaces*, 2018, **10**, 29435–29447.
- Y. Chen, C. Li, J. Zhou, S. Zhang, D. Rao, S. He, M. Wei, D. G. Evans and X. Duan, *ACS Catal.*, 2015, **5**, 5756–5765.
- M. Kołodziej, A. Drelinkiewicz, E. Lalik, J. Gurgul, D. Duraczyńska and R. Kosydar, *Appl. Catal., A*, 2016, **515**, 60–71.
- C. Volckmar, M. Bron, U. Bentrup, A. Martin and P. Claus, *J. Catal.*, 2009, **261**, 1–8.
- Q. Hu, S. Wang, Z. Gao, Y. Li, Q. Zhang, Q. Xiang and Y. Qin, *Appl. Catal., B*, 2017, **218**, 591–599.
- J. Zhao, X. Xu, X. Li and J. Wang, *Catal. Commun.*, 2014, **43**, 102–106.
- R. Nie, J. Wang, L. Wang, Y. Qin, P. Chen and Z. Hou, *Carbon*, 2012, **50**, 586–596.
- Z. Cao, J. Bu, Z. Zhong, C. Sun, Q. Zhang, J. Wang, S. Chen and X. Xie, *Appl. Catal., A*, 2019, **578**, 105–115.
- E. Plessers, D. E. De Vos and M. B. J. Roeffaers, *J. Catal.*, 2016, **340**, 136–143.
- L. Bromberg, Y. Diao, H. Wu, S. A. Speakman and T. A. Hatton, *Chem. Mater.*, 2012, **24**, 1664–1675.
- S. Yuan, L. Zou, J.-S. Qin, J. Li, L. Huang, L. Feng, X. Wang, M. Bosch, A. Alsalmé, T. Cagin and H.-C. Zhou, *Nat. Commun.*, 2017, **8**, 15356.
- Y. Chen, Y. Zhou, H. Wang, J. Lu, T. Uchida, Q. Xu, S. Yu and H. Jiang, *ACS Catal.*, 2015, **5**, 2062–2069.
- G. Ferey, C. Mellot-Draznieks, C. Serre, F. Millange, J. Dutour, S. Surblé and I. Margiolaki, *Science*, 2005, **309**, 2040–2042.
- H. Pan, X. Li, Y. Yu, J. Li, J. Hu, Y. Guan and P. Wu, *J. Mol. Catal. A: Chem.*, 2015, **399**, 1–9.
- K. Leng, Y. Sun, X. Li, S. Sun and W. Xu, *Cryst. Growth Des.*, 2016, **16**, 1168–1171.
- H. Liu, Z. Li and Y. Li, *Ind. Eng. Chem. Res.*, 2015, **54**, 1487–1497.
- A. Nagendiran, V. Pascanu, A. Bermejo Gómez, G. González Miera, C.-W. Tai, O. Verho, B. Martín-Matute and J.-E. Bäckvall, *Chem. – Eur. J.*, 2016, **22**, 7184–7189.
- D. Yin, H. Ren, C. Li, J. Liu and C. Liang, *Chin. J. Catal.*, 2018, **39**, 319–326.
- H. Liu, L. Chang, L. Chen and Y. Li, *ChemCatChem*, 2016, **8**, 946–951.
- V. R. Bakuru and S. B. Kalidindi, *Chem. – Eur. J.*, 2017, **23**, 16456–16459.
- Z. Guo, C. Xiao, R. V. Maligal-Ganesh, L. Zhou, T. W. Goh, X. Li, D. Tesfagaber, A. Thiel and W. Huang, *ACS Catal.*, 2014, **4**, 1340–1348.

- 46 Y. Fu, Y. Guo, Y. Guo, Y. Wang, L. Wang, W. Zhan and G. Lu, *Catal. Sci. Technol.*, 2017, **7**, 4136–4144.
- 47 H. Wang, S. Bai, Y. Pi, Q. Shao, Y. Tan and X. Huang, *ACS Catal.*, 2019, **9**, 154–159.
- 48 M. Zhu, B. Huang, Q. Shao, Y. Pi, Y. Qian and X. Huang, *ChemCatChem*, 2018, **10**, 3214–3218.
- 49 S. Wei, Y. Zhao, G. Fan, L. Yang and F. Li, *Chem. Eng. J.*, 2017, **322**, 234–245.
- 50 S. Zhang, G. Zhan, X. Wang, S. Cao, Q. Yang, L. Yang, M. Li, J. Han, X. Zhu, H. Wang, X. Liu and L. Zhang, *Appl. Catal., B*, 2010, **269**, 118782.
- 51 W. Huang, Q. Zhang, D. Zhang, J. Zhou, C. Si, L. Guo, W. Chu and Z. Wu, *J. Phys. Chem. C*, 2013, **117**, 6872–6879.
- 52 A. Han, J. Zhang, W. Sun, W. Chen, S. Zhang, Y. Han, Q. Feng, L. Zheng, L. Gu, C. Chen, Q. Peng, D. Wang and Y. Li, *Nat. Commun.*, 2019, **10**, 3787.
- 53 R. Li, W. Yao, Y. Jin, W. Jia, X. Chen, J. Chen, J. Zheng, Y. Hu, D. Han and J. Zhao, *Chem. Eng. J.*, 2018, **351**, 995–1005.
- 54 Z. Tian, C. Liu, Q. Li, J. Hou, Y. Li and S. Ai, *Appl. Catal., A*, 2015, **506**, 134–142.
- 55 Q. Wang, G. Wang, H. Xin, J. Liu, G. Xiong, P. Wu and X. Li, *Catal. Sci. Technol.*, 2019, **9**, 3226–3237.
- 56 N. M. Bertero, A. F. Trasarti, B. Moraweck, A. Borgna and A. J. Marchi, *Appl. Catal., A*, 2009, **358**, 32–41.
- 57 M. Armbrüster, G. Wowsnick, M. Friedrich, M. Heggen and R. Cardoso-Gil, *J. Am. Chem. Soc.*, 2011, **133**, 9112–9118.
- 58 Q. Feng, S. Zhao, Y. Wang, J. Dong, W. Chen, D. He, D. Wang, J. Yang, Y. Zhu, H. Zhu, L. Gu, Z. Li, Y. Liu, R. Yu, J. Li and Y. Li, *J. Am. Chem. Soc.*, 2017, **139**, 7294–7301.
- 59 W. O. Oduro, N. Cailuo, K. M. K. Yu, H. Yang and S. C. Tsang, *Phys. Chem. Chem. Phys.*, 2011, **13**, 2590.
- 60 Y. Dai, X. Gao, X. Chu, C. Jiang, Y. Yao, Z. Guo, C. Zhou, C. Wang, H. Wang and Y. Yang, *J. Catal.*, 2018, **364**, 192–203.
- 61 S. Yuan, L. Feng, K. Wang, J. Pang, M. Bosch, C. Lollar, Y. Sun, J. Qin, X. Yang, P. Zahng, Q. Wang, L. Zou, Y. Zhang, L. Zahang, Y. Fang, J. Li and C. Zhou, *Adv. Mater.*, 2018, **30**, 1704303.